International Forum on Aeroelasticity and Structural Dynamics
IFASD 2024
17-21 June 2024, The Hague, The Netherlands

INFLUENCE OF NONLINEAR AERODYNAMIC EFFECTS ON HIGH ASPECT RATIO AIRCRAFT MODEL

Álvaro A. G. Quesada[1], Pedro J. González[1], Guilherme C. Barbosa[1], Gerrit Stavorinus[1], Flávio J. Silvestre[1]

[1]Technical University of Berlin
Marchstraße 12, 10587 Berlin, Germany
garcia.quesada@tu-berlin.de
p.gonzalez.ramirez@tu-berlin.de
g.chaves.barbosa@tu-berlin.de
g.stavorinus@tu-berlin.de
flavio.silvestre@tu-berlin.de

Keywords: High Aspect Ratio, Modeling, Aerodynamic Nonlinearities, Stall, Follower Forces

Abstract:

This paper studies the influence of stall effects and follower forces on High Aspect Ratio (HAR) aircraft model for different load cases and aircraft flexibility levels. The Modeling and Simulation Group Toolbox created by the Chair of Flight Mechanics, Flight Control and Aeroelasticity of Technical University Berlin (ModSiG-FMRA) is used for modeling and analyzing the aerodynamic nonlinearities on the TU-Flex aircraft model. TU-Flex is a scaled flight demonstrator embodying a HAR transport aircraft configuration with modular construction, allowing different flexibility levels (for instance, in this paper a flexible and very flexible set). The ModSiG-FMRA framework uses mean axes formulation, modal superposition for structural dynamics, therefore considered linear, nonlinear flight mechanics, and quasi-steady or unsteady strip theory for incremental aerodynamics due to elastic deformations. The aerodynamic formulation permits to incorporate stall effects and/or follower forces. The follower forces effect does not show an influence on the load cases simulations of the TU-Flex flight envelope while considering geometrically linear structure. On the other side, stall effects influence the TU-Flex dynamic behaviour by the coupling rigid body and structure, not captured by linear aerodynamics formulations. This coupling mechanism is emphasised by increasing the flexibility level.

1 INTRODUCTION

The drive to mitigate environmental impacts in aviation has pushed aircraft wing designs towards lighter-weight structures and increased aspect ratio [1]. The high flexibility of these wings under specific flight conditions results in pronounced deflections and strong coupling between flight dynamics and aeroelasticity, and may lead to aerodynamic nonlinearities. Consequently, addressing these challenges requires the development of appropriate formulation to this dynamical problem, capable of accurately predicting these effects while maintaining computational efficiency suitable for aircraft design applications.

Waszak and Schmidt [2], already observed that by reducing the structural rigidity of an already existing flexible aircraft, the rigid body modes become closer in frequency to structural dynamic modes. The authors developed the nonlinear equations of motion for an elastic airplane,

applying mean axes formulation and using modal decomposition coupled with 2D strip theory incompressible quasi-steady aerodynamics. Silvestre and Paglione [3], following the same methodology, added the aerodynamic influence coefficients description for the lateral motion, and with contribution of all lifting surfaces (horizontal and vertical empennage). Van Schoor et al. [4] concluded the need of including aeroelastic effects of High Altitude Long Endurance (HALE) aircraft in control design due to alterations of aeroelastic modal coupling with altitude. The authors carried out an aeroelastic analysis using a linear structural model based on modal approach, and comparing the aircraft stability implementing 2D quasi-steady and unsteady strip theory aerodynamics. Patil and Hodges [5] studied the causes of NASAs Helios mishap [6] analysing the flight dynamics stability of the very flexible flying wing. The study included a root locus varying payload, obtaining a significant change in the flight dynamics and elastic modes, because of the change in the shape (dihedral), potentially leading to the unstable phugoid motion. The authors consider geometrically-exact beam theory [7, 8] with large motion airfoil aerodynamic theory. The computation of unsteady aerodynamic loads is based on finite-state airloads models [9].

Regarding the consideration of aerodynamic nonlinearities on HAR aircraft modeling, Patil et al. [10] carried out a nonlinear aeroelastic analysis of complete aircraft in subsonic flow, considering unsteady flow behaviour and dynamic stall. They supported the implementation of stall effects, since HALE aircraft flight at high altitude (low density) and low speed (consequently low dynamic pressure), needing greater angles of attack values to lift, and thus operating close to the stall point. Besides, HAR wings present large deformations, being possible to encounter stall at the wingtip. For this purpose, a 2D finite state inflow theory was implemented, including compressibility effects and dynamic stall according to ONERA approach [9]. It could be shown that the consideration of the dynamic stall led to a change of the onset flutter speed for high angles of attack and Limit-Cycle Oscillations (LCO). Subsequently, Su and Cesnik [11] in their analysis of dynamic response of highly flexible flying wings also implemented 2-D finite state unsteady subsonic aerodynamics [9] with two different simplified stall models which consist of: after reaching the stall angle of attack a constant lift coefficient is kept and the longitudinal moment coefficient is constant too (stall model 1); or after reaching the stall angle of attack a constant lift coefficient is kept and the longitudinal moment coefficient drops down to another constant value, producing a downwards pitch moment (stall model 2). The authors concluded that the effects of considering stall have a significant impact on transient responses of the wing and could alter the vehicle flight behaviour.

Another nonlinearity within the aerodynamic model is follower aerodynamic forces which consists of implementing the aerodynamic loads on the beam reference system attached to the wing structure on the current deformed shape, instead of being implemented on the undeformed shape. Riso and Cesnik [12] investigated the geometrically nonlinear effects in the aeroelastic behaviour of a very flexible wing, showing how neglecting follower loads for vertical wingtip displacement greater than 10-15$\%$ (for the static aeroelastic analysis, i.e. in a constant flight condition), it would yield an underestimation of 10% of the wingtip vertical displacement comparing with the fully nonlinear model (follower aerodynamic loads and nonlinear kinematics, i.e capturing shortening and curvature structure effects). Nevertheless, neglecting the shortening and curvature effects (linear kinematics) the consideration of follower forces do not have any influence on the static aeroelastic response.

The objective of this paper is to verify the influence of the aerodynamic nonlinearities (stall effects and follower forces) on a HAR aircraft demonstrator model, as the level of flexibility

increases. To represent the intensified coupling resulting from increased wing flexibility, the study focuses on the TU-Flex platform. It is a scaled flight demonstrator embodying a HAR transport aircraft configuration. The aircraft design is characterized by a modular construction, facilitating the direct exchange of wings with different configurations. In its initial version, the aircraft is configured with a Flexible Wing (FW) set, allowing for wingtip deflections up to 10% of the wings semi-span for manoeuvre input or external excitation at load factor 1.5g. Additionally, the aircraft can accommodate a Very Flexible Wing (VFW) set, extending wingtip deflections up to 20% at load factor 1.5g. The increase of the wing flexibility yields a decrease of structural modes frequency, resulting in a stronger coupling between rigid body and elastic modes [13]. In Section 2 the reference aircraft is described. The following Sections 3 and 4 explain the used numerical framework and its modeling formulations respectively. The results regarding stability analyses and dynamic behaviour of the TU-Flex aircraft model (FW and VFW configuration) using different aerodynamic formulations are discussed in Section 5. The study conclusions are explained in Section 6.

2 TU-FLEX AIRCRAFT

TU-Flex is a new flight demonstrator with a transport aircraft configuration and HAR wings, designed in collaboration between the Chair of Flight Mechanics, Flight Control and Aeroelasticity of Technical University Berlin (FMRA-TUB) and the Institute of Aeroelasticity of the German Aerospace Center (DLR-AE). This platform allows for gathering coupled experimental data of both flight and structural dynamics of the aircraft. With a design that permits easy wing exchange, the aircraft can be tested with different wing sets with variable (increasing) level of flexibility. So far the half-span FW has been already built and wind tunnel tests have been carried out in the Crosswind Simulation Facility (SWG) of the DLR-AE in Göttingen [14].

The initial model of TU-Flex with preliminary design wings was created in OpenVSP [15] and then imported in Altair HyperMesh [16] to generate the final Finite Element (FE) model of the fuselage and tail assembly [17]. The structural FE model and aerodynamics Doublet Lattice Method (DLM) of the wing sets (FW and VFW) were generated using the in-house software ModGen [18, 19] at the DLR-AE [17, 20]. Fig. 1 shows the TU-Flex aircraft FE model, using MSC Nastran as the FE solver. Most of the structure of TU-Flex is made up of thin walled composite laminate, so shell elements (CQUAD4 and CTRIA3) are the most common type of FE used. The foam filling of the wing and tail assembly is modeled with solid elements (CHEXA and CPENTA). The landing gear and the support beam with the fuselage are modeled with beam elements (CBEAM). The internal systems and the two ducted fan motors were modeled as concentrated mass elements (CONM2), assigned to grid points at their center of gravity. They were connected to the rest of the structure with interpolation elements (RBE3). Altogether, the model contains approximately 36,000 degrees of freedom. In Table 1 and 2, the frequencies of the first eight modes (considered in this paper) for the TU-Flex model with FW and VFW set are represented respectively. The higher the structure flexibility is, the lower the structure mode frequencies are. In particular, the W1SBO mode for the TU-Flex with VFW set is 0.23Hz higher than the Short Period rigid body mode.

With the purposes of aircraft design and control application, a low-order TU-Flex aircraft model is generated. In the following, a description of the used numerical framework and its modeling formulations is described. A control evaluation of this low-order TU-Flex aircraft model is given in [21].

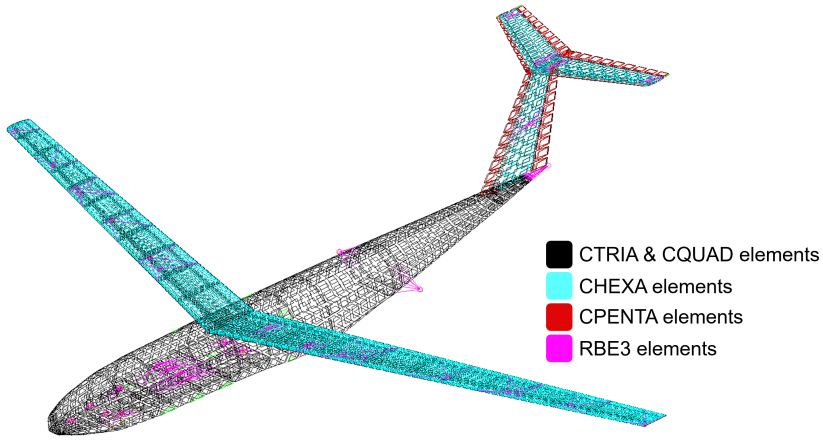

Figure 1: TU-Flex structural FE model (image from Ref. [17]).

Table 1: TU-Flex aircraft FE model modal frequencies with FW set.

#	Mode type	Label	Frequency (Hz)
1	Wing 1^{st} Symmetric Bending Out-of-Plane	W1SBO	4.73
2	Wing 1^{st} Asymmetric Bending Out-of-Plane	W1ABO	7.89
3	Wing 2^{nd} Asymmetric Bending Out-of-Plane + Vertical Empennage 1^{st} Bending Out-of-Plane	W2ABO-V1BO	12.87
4	Wing 2^{nd} Symmetric Bending Out-of-Plane + Horizontal Empennage 1^{st} Symmetric Bending Out-of-Plane	W2SBO-H1SBO	17.29
5	Wing 2^{nd} Asymmetric Bending Out-of-Plane + Vertical Empennage 1^{st} Torsion	W2ABO-V1T	19.18
6	Horizontal Empennage 1^{st} Asymmetric Bending Out-of-Plane + Vertical Empennage 1^{st} Torsion	H1SBO-V1T	19.8
7	Fuselage 1^{st} Bending Out-of-Plane + Horizontal Empennage 1^{st} Symmetric Bending Out-of-Plane	F1BO-H1SBO	21.83
8	Vertical Empennage 1^{st} Torsion + Wing 1^{st} Asymmetric Bending In-Plane	V1T-W1ABI	24.54

3 COMPUTATIONAL FRAMEWORK

The study uses the Modeling and Simulation Group Toolbox created by the FMRA-TUB, a low-order framework for modeling, analyzing, and simulating very flexible/flexible wings and aircraft (ModSiG-FMRA). ModSiG-FMRA models aircraft using the mean axes formulation where the linear and angular momentum caused by deformations are zero. The Mean Axes Reference Frame (MARF) origin is located at the aircraft Centre of Gravity (CG) and parallel to the typical flight mechanics reference frame: x-axis lying in the fuselage longitudinal axis, pointing to the aircrafts nose; z-axis lying in the aircraft vertical plane of symmetry (the aircraft is assumed to have a right-left symmetry), pointing down; and y-axis completing the right-hand Cartesian coordinate system.

To represent the aircraft structural dynamics the modal superposition technique is used, transforming from the six degrees of freedom per element to the so called modal eigenforms [2,3,22].

Table 2: TU-Flex aircraft FE model modal frequencies with VFW set.

#	Mode type	Label	Frequency (Hz)
1	Wing 1^{st} Symmetric Bending Out-of-Plane	W1SBO	1.69
2	Wing 2^{nd} Asymmetric Bending Out-of-Plane	W2ABO	4.59
3	Wing 2^{nd} Asymmetric Bending Out-of-Plane + Vertical Empennage 1^{st} Bending Out-of-Plane	W2ABO-V1BO	9.4
4	Wing 1^{st} Symmetric Bending In-Plane + Wing 2^{nd} Symmetric Bending Out-of-Plane	W1SBI-W2SBO	10.46
5	Wing 2^{nd} Symmetric Bending Out-of-Plane	W2SBO	10.55
6	Wing 2^{nd} Asymmetric Bending Out-of-Plane + Wing 1^{st} Asymmetric Bending In-Plane + Vertical Empennage 1^{st} Torsion	W2ABO-W1ABI-V1T	12.64
7	Wing 2^{nd} Asymmetric Bending Out-of-Plane + Vertical Empennage 1^{st} Bending Out-of-Plane + Vertical Empennage 1^{st} Torsion	W2ABO-V1BO-V1T	16.31
8	Horizontal Empennage 1^{st} Symmetric Bending Out-of-Plane + Fuselage 1^{st} Bending Out-of-Plane	H1SBO-F1BO	21.77

Thus, the aircraft deformation $\mathbf{p_d}$ can be written using modal superposition as the following equation

$$\mathbf{p_d}|_{B^{(G)}}(x,y,z,t) = \mathbf{\Phi}(x,y,z)\eta(t) \tag{1}$$

where $\mathbf{\Phi}_{3xn_e}$ is the modal matrix being n_e the number of elastic modes of the free-body undamped vibration problem, and $\eta_{n_e x1}$ is the vector of the modal amplitudes. The aicraft equations of motion used by ModSiG-FMRA are

$$\begin{aligned}
\dot{\mathbf{V}}|_{B^{(G)}} &= -\omega|_{B^{(G)}} \times \mathbf{V}|_{B^{(G)}} + \mathbf{T}_{B^{(G)I}}\mathbf{G}|_I + \frac{1}{m}\mathbf{F^{ext}}|_{B^{(G)}}, \\
\dot{\omega}|_{B^{(G)}} &= -\mathbf{J^{-1}}(\omega|_{B^{(G)}} \times (\mathbf{J}\omega|_{B^{(G)}})) + \mathbf{J^{-1}}\mathbf{M^{ext}}|_{B^{(G)}}, \\
\ddot{\eta} &= -2\xi\omega_\mathbf{n}\dot{\eta} - \omega_\mathbf{n}^\mathbf{2}\eta + \mu^{-\mathbf{1}}\mathbf{Q}_\eta
\end{aligned} \tag{2}$$

The first two vectorial equations represent the linear and angular velocities' differential equations of the classic rigid-body flight dynamics. The third equation consists of the aeroelastic dynamics in modal coordinates where η is the modal amplitudes vector; μ and $\omega_\mathbf{n}$ are diagonal matrices of the n_e modal masses μ_i and undamped natural frequencies $\omega_{n,i}$; ξ is the matrix of the n_e structural modal damping ratios ξ_i; and Q_η is the vector of the n_e generalized loads Q_{η_i} of each elastic mode [22].

The aerodynamic forces and moments placed at $\mathbf{F^{ext}}|_{B^{(G)}}$ and $\mathbf{M^{ext}}|_{B^{(G)}}$, and aerodynamic generalized loads Q_η from Eq. 2 can be computed within the ModSiG-FMRA framework using different approaches. Incremental aerodynamics in incompressible flow due to elastic deformations are modeled in the time domain, applying strip theory at different complexity levels (in Section 4.2 a detailed description of the different formulations is given). In the following subsections, an overview of the discretization method of a MSC Nastran model to use strip theory as well as the workflow of the ModSiG-FMRA framework is given.

3.1 Structural Discretization

The strip theory considers structural linear vertical displacements (along the z-axis of MARF), neglecting chordwise deformation, assuming lifting surfaces (wing, horizontal and vertical empennage) as flat plates. The aircraft model lifting surfaces from MSC Nastran are three-dimensional, filled with solid elements (Fig. 1), needing to choose a surface to model them by strip theory. Regarding TU-Flex, the upper surface of each lifting surface has been approximated as a flat plate. In Fig. 2, the disposition of the TU-Flex wing upper surface structural nodes and mid chord nodes are represented.

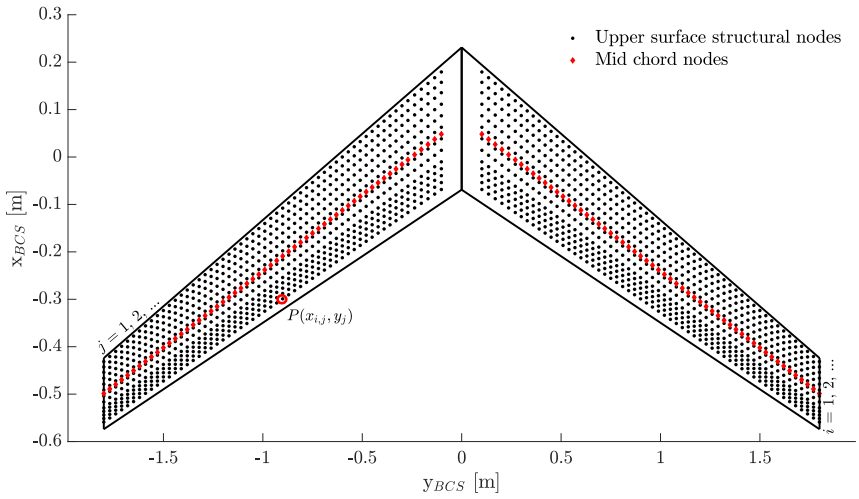

Figure 2: TU-Flex wing upper surface structural nodes and mid chord nodes.

By the linear structural displacements theory, the equivalent vertical elastic displacement $h_k^f(x_{i,j}, y_j)$ of any point $P(x_{i,j}, y_j)$ on the lifting surface for the kth elastic mode can be approximately represented as a composition of the vertical displacement $\varphi_k^{LRA}(y_j)$ and torsion $\gamma_k^{LRA}(y_j)$ of points placed at a Load Reference Axes (LRA) of the corresponding lifting surface as the following

$$h_k^f(x_{i,j}, y_j) = \varphi_k^{LRA}(y_j) + (x_{i,j} - x_{LRA_j})\gamma_k^{LRA}(y_j) \tag{3}$$

In Fig. 2, the subscripts i and j are the structural node row chordwise and structural node column spanwise respectively. For the TU-Flex, the mid chord line corresponds to the LRA. The equivalent vertical elastic displacement $h_k^f(x_i, y_j)$ corresponds to the third translation component of the eigenvector relative to the kth elastic mode. The computation of the vertical displacement $\varphi_k^{LRA}(y_j)$ and torsion $\gamma_k^{LRA}(y_j)$ at the LRA for the kth elastic mode is carried out through the optimization of the Eq. 3 written as the following

$$0 = \varphi_k^{LRA}(y_j) + (x_{i,j} - x_{LRA_j})\gamma_k^{LRA}(y_j) - h_k^f(x_{i,j}, y_j) \tag{4}$$

The vertical displacement $h_k^f(x_i, y_j)$ is obtained from the MSC Nastran modal analysis (SOL103). Knowing the position of the lifting surface structural nodes $x_{i,j}$ and the LRA nodes x_{LRA_j}, an overdetermined set of n_i equations for the jth structural nodes column and kth elastic mode is obtained. According to the aerodynamic discretization of the aerodynamic distribution provided

by the user, the framework will interpolate the structural nodes to the aerodynamic centre position per aerodynamic strip. In Fig. 3, the structural and aerodynamic discretization for TU-Flex wing is depicted. Same procedure is carried out for the vertical and horizontal empennages.

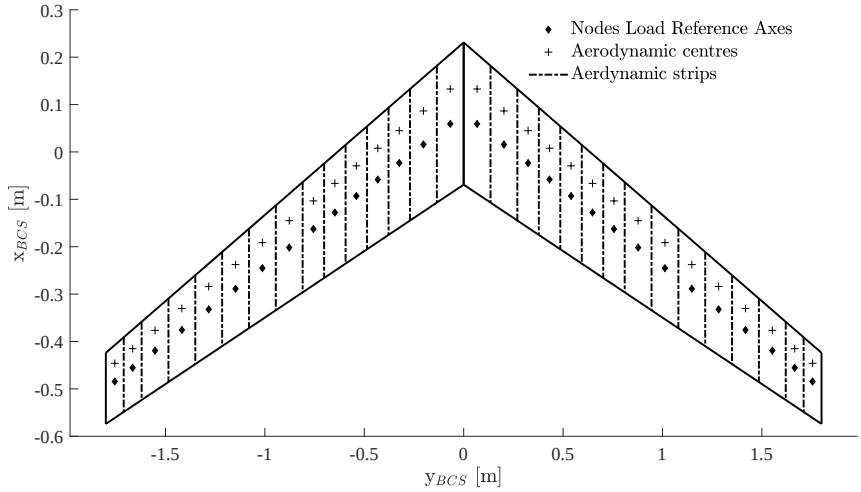

Figure 3: TU-Flex wing upper surface structural nodes and mid chord nodes.

3.2 Workflow

In Fig. 4 the workflow of the numerical framework ModSiG-FMRA is represented. The fact of using the modal superposition technique for representing the aircraft structural dynamics implies the definition of the aircraft modal basis as input of ModSiG-FMRA framework. Applying the SOL103 in MSC Nastran of the corresponding aircraft model, the modal analysis is carried out. The output file ".f06" of this SOL103 contains the undamped natural frequencies $\omega_{n,i}$ and inertia parameters required for Eq. 2, and the third translation component of the structural nodes eigenvectors $h_k^f(x_{i,j}, y_j)$ for the kth elastic mode required for Eq. 4. The SOL103 output file ".bdf" is another input of the framework, since it is used for the structural discretization (Section 3.1) in Eq. 4, consisting of the structural nodes position $x_{i,j}$. Applying the optimization described in Section 3.1, the necessary modal basis of the LRA ($\varphi_k^{LRA}(y_j)$ and $\gamma_k^{LRA}(y_j)$) for the y_j structural nodes position is obtained.

Strip theory is used to model the aircraft aerodynamics, requiring the distributed aerodynamics of the lift and control surfaces as framework inputs. According to this distribution, the modal basis of the LRA ($\varphi_k^{LRA}(y_j)$ and $\gamma_k^{LRA}(y_j)$) according to the structural nodes positions is interpolated at the aerodynamic centres y_{AC_j}, obtaining $\varphi_k^{LRA}(y_{AC_j})$ and $\gamma_k^{LRA}(y_{AC_j})$. The propulsive properties such as engine thrust functions, angular attitude and position requires to be predefined. In this study the TU-Flex engine thrust functions have been set according to [23]. The general geometric parameters of the lifting surfaces such as span, chord distribution, and areas are defined as framework inputs. Selecting the low-order aerodynamic modeling formulation (described in Section 4.2) and defining the trimming and simulation conditions, the trimming routine can be performed on Matlab using *fsolve* function. The state vector for this routine is

$$\mathbf{X} = [V, \theta, H, \alpha, q, \beta, r, \phi, p, \Psi, x_e, y_e, \eta, \dot{\eta}, \lambda_\mathbf{1}, \lambda_\mathbf{2}] \tag{5}$$

where V is the velocity; θ is the pitch Euler angle; H is the altitude; α is the angle of attack; q is the pitch rate; β is the slip angle; r is the yaw angular velocity; ϕ is the roll Euler angle;

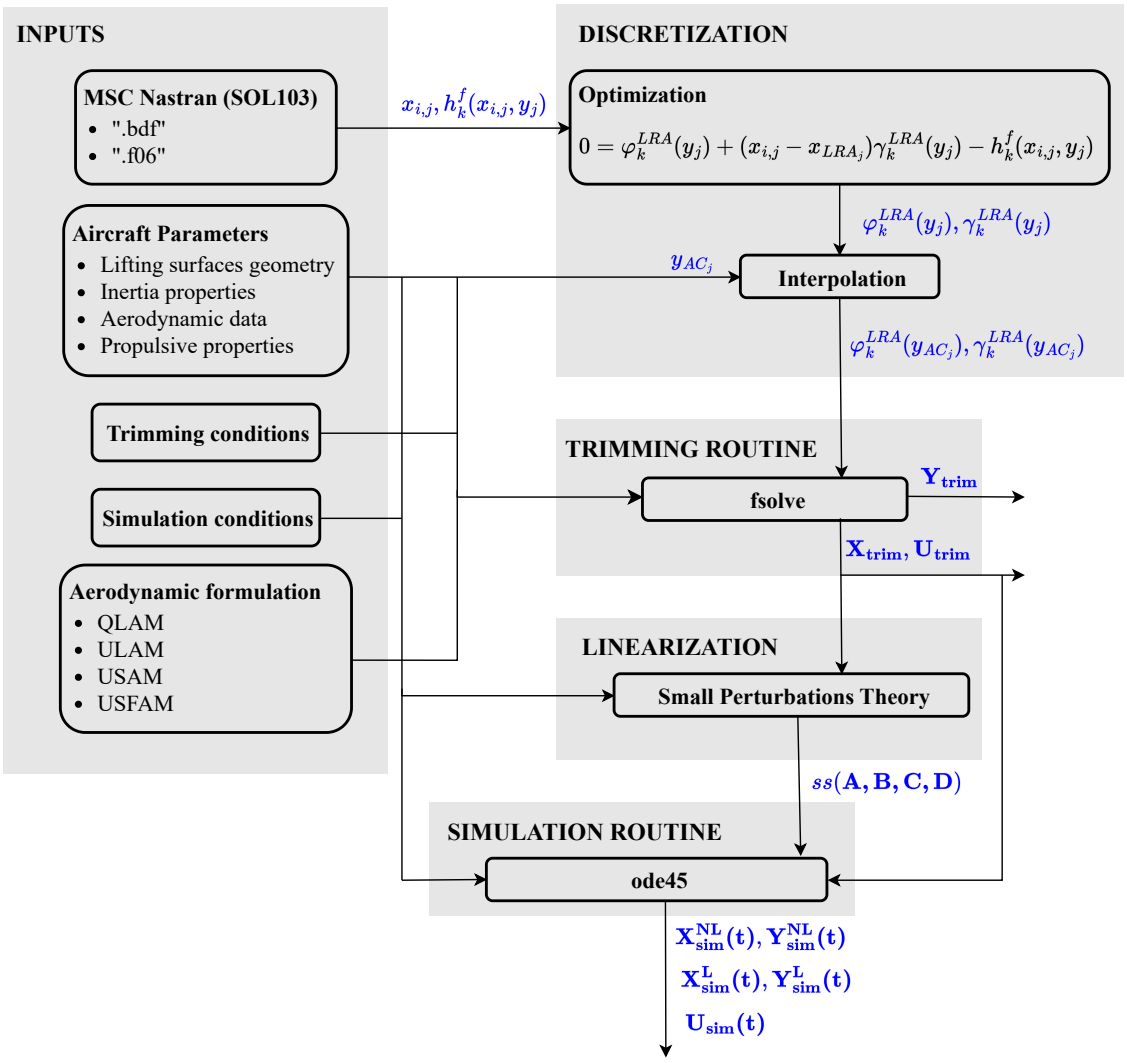

Figure 4: ModSiG-FMRA framwork workflow.

p is the roll angular velocity; Ψ is the yaw Euler Angle; x_e is the x trajectory coordinate in the Earth Reference Frame (ERF, considered as the Inertial Reference Frame); y_e is the y trajectory coordinate in the ERF; η and $\dot{\eta}$ are the elastic modal shapes and its derivatives (each vector consists of as many positions as number of modes considered); λ_1 and λ_2 are the lag states due to airfoil arbitrary motion (each vector consists of as many positions as number of aerodynamic strips). The input vector is

$$\mathbf{U} = [m, \delta_e, \delta_{ai,r}, \delta_{ai,l}, \delta_{am,r}, \delta_{am,l}, \delta_{ae,r}, \delta_{ae,l}, \delta_{f,r}, \delta_{f,l}, \delta_r, \delta_T, w_x, w_y, w_z] \tag{6}$$

where m is the aircraft mass; δ_e is the elevator deflection; $\delta_{ai,r}$ and $\delta_{ai,l}$ are the left and right inner aileron deflections; $\delta_{am,r}$ and $\delta_{am,l}$ are the left and right mid aileron deflections; $\delta_{ae,r}$ and $\delta_{ae,l}$ are the left and right external aileron deflections; $\delta_{f,r}$ and $\delta_{f,l}$ are the left and right flap deflections; δ_r is the rudder deflection; δ_T is the throttle per engine; and w_x, w_y and w_z are the wind components in ERF. The computed outputs can be defined according to the needs of the user. For this study the distributed deformations (vertical displacement and twist angle) along the wing span as well as the own state vector has been defined as output vector $\mathbf{Y}$.

Linearizing through the theory of small perturbations, the state space matrices of the system

(A,B,C,D) are obtained. The nonlinear dynamics system of Eq. 2 (adding the lag states dynamics in case of unsteady aerodynamics) defined in Matlab will be run from Simulink using *S-Function*. The linear dynamics system will be also integrated throughout time using the state space matrices, computing the outputs according to the observation matrix.

4 NUMERICAL MODEL

In this section, the modeling formulations of the aircraft structural dynamics used by the numerical framework described in Section 3 is presented. The numerical model is set to one structure formulation and four complexity levels to model the aerodynamics. The theoretical basis of them is described in the following.

4.1 Low-order Structural Modeling

The low-order structural model consists of geometrically linear structure, representing the aircraft structure deformation by modal superposition (Eq. 1) [2, 3, 22]. The aircraft model is reduced to its lifting surfaces, simplifying them as LRAs (Section 3.1). Neglecting the chordwise deformation of the lifting surfaces, the lifting surface deformed shape is approximately represented by a composition of bending and torsion deformation of the corresponding LRA lifting surface (Eq. 3). Applying modal superposition technique, summing up for all n_e chosen elastic modal shapes η_k, the equivalent plunge and pitching movement at the LRA are given by

$$\begin{aligned} h^f(x_{LRA_j}, y_j, t) &= \sum_{k=1}^{n_e} \varphi_k^{LRA}(y_j)\eta_k(t), \\ \alpha^f(x_{LRA_j}, y_j, t) &= \sum_{k=1}^{n_e} -\gamma_k^{LRA}(y_j)\eta_k(t) \end{aligned} \tag{7}$$

4.2 Low-order Aerodynamic Modeling

The low-order aerodynamic modeling frame consists of four formulations based on incompressible strip theory: quasi-steady linear aerodynamics, unsteady linear aerodynamics, unsteady aerodynamics with stall effects, and unsteady aerodynamics with stall effects and follower forces.

4.2.1 Linear Aerodynamics Models (QLAM and ULAM)

The Quasi-steady Linear Aerodynamics Model (QLAM) is based on incompressible quasi-steady strip theory, modeling the incremental aerodynamic loads due to structural deformations as in [2, 3]. The Unsteady Linear Aerodynamics Model (USAM) models unsteady incremental aerodynamics due to elastic deformations in time domain, using strip theory and indicial function following [22]. For both models the linear aerodynamics assumption considers that the local $cl_{\alpha,j}$ per strip is constant with the local AoA. For the TU-flex reference aircraft the local $cl_{\alpha,j}$ has been computed using the data XFOIL of the corresponding wing airfoil. Computing the interpolation line that joins $cl(\alpha = -3^o)$ with $cl(\alpha = 4.5^o)$, a linear lift polar is obtained. Extracting the slope of this linear lift polar, the local $cl_{\alpha,j}$ per strip is obtained. Considering that the TU-Flex airfoils does not change along the span of the corresponding lifting surface, the local cl_α (or cl_β) is equal for all the strips of the respective lifting surface.

4.2.2 Unsteady Stall Aerodynamics Model (USAM)

Unsteady Stall Aerodynamics Model (USAM) follows ULAM formulation with a difference in the local lift slope $cl_{\alpha,j}$ to simulate a local stall effect. For the QLAM and ULAM, the local $cl_{\alpha,j}$ is constant. The USAM uses a local $cl_{\alpha,j}(\alpha_j)$ for the jth strip that is function of the local angle of attack α_j of the corresponding strip (this local angle of attack being the sum between the rigid body AoA and the one due to deformation). This function was computed using the lift polar from XFOIL of the used airfoil for the corresponding lifing surface. Computing a smooth cubic spline of the lift polar using the points series from XFOIL, the $cl_{\alpha,j}(\alpha_j)$ is obtained deriving the resultant polynomial. This $cl_{\alpha,j}(\alpha_j)$ (or $cl_{\beta,j}(\beta_j)$ in case of the vertical empennage) function has been implemented for the wing, and vertical and horizontal empennages.

With the purpose of a better understanding of the comparison between the linear aerodynamics models (ULAM and QLAM) and the USAM, this paper will include the Unsteady Quasi-nonlinear Aerodynamics Model (UQNAM). The UQNAM uses a local $cl_{\alpha,j}(\alpha_j)$ which is a function of the local angle of attack from -5^o to 7^o. Outside of this range the function takes the limit values, i.e $cl_{\alpha,j}$ equals $cl_{\alpha,j}(-5)$ for local AoA smaller than -5^o and $cl_{\alpha,j}$ equals $cl_{\alpha,j}(7)$ for local AoA greater than 7^o. The aim of this model is to facilitate the comprehension of which effects come from considering nonlinear the "linear lift polar regime" and which effects come from the stall regime where $cl_{\alpha,j}$ is close to zero or even negative. Therefore the UQNAM and USAM will be different once the local angle of attack of a certain lifting surface strip takes a value outside the range [-5,7] degrees. In Fig. 5 the lift polar for the TU-Flex wing airfoil for QLAM/ULAM, UQNAM and USAM and their respective cl_α is represented.

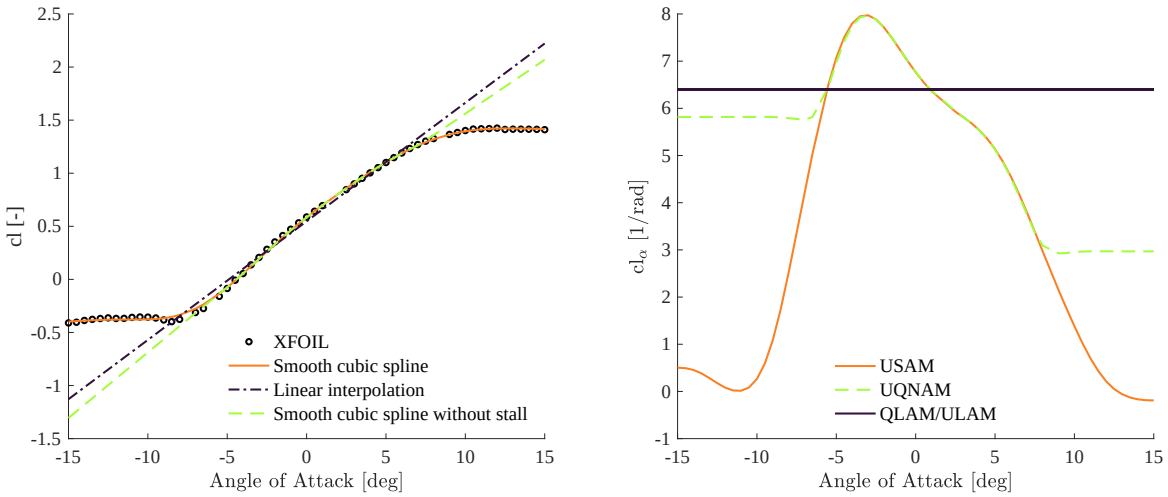

Figure 5: Lift polar for the TU-Flex wing airfoil for QLAM/ULAM, UQNAM and USAM and their respective cl_α.

4.2.3 Unsteady Stall Follower Forces Aerodynamics Model (USFAM)

The Unsteady Stall Follower Forces Aerodynamics Model (USFAM) uses the unsteady aerodynamics with the local $cl_{\alpha,j}(\alpha_j)$ function of the USAM, including the aerodynamic nonlinear effect of follower forces. Considering the bending out-of-plane deformation, the incremental lift force per strip computed according to [22] are obtained along the z-axis normal to the corresponding surface strip. In Fig. 6 the dihedral deformation angle Γ_j corresponding to the jth aerodynamic strip due to bending out-of-plane deformation is depicted. This angle represents the rotation between the local aerodynamic reference frame (LARF) $O_{A^{(L)}}$ described in [22] and a local normal aerodynamic reference frame (LNARF) $O_{NA^{(L)},j}$ with origin at the aerody-

namic centre of the jth aerodynamic strip. Thus the dihedral deformation angle Γ_j of the jth aerodynamic strip is given by

$$\Gamma_j(t) = \arctan \frac{h^f(x_{AC_j}, y_{2,j}, t) - h^f(x_{AC_j}, y_{1,j}, t)}{\Delta y_j} \tag{8}$$

where Δy_j is the aerodynamic width strip (considered constant since geometrically linear structure is applied); and $h^f(x_{AC_j}, y_{1,j}, t)$ and $h^f(x_{AC_j}, y_{2,j}, t)$ are the plunge deformation of the jth aerodynamic strip borders at the aerodynamic centre position position of the corresponding strip. The plunge deformations at those points are computed combining the linear deformations approach (Eq. 3) and modal superposition technique (Eq. 7) by the following

$$h^f(x_{AC_j}, y_j, t) = \sum_{k=1}^{n_e} (\varphi_k^{LRA}(y_j) + (x_{AC_j} - x_{LRA_j})\gamma_k^{LRA}(y_j))\eta_k(t) \tag{9}$$

Therefore for each time instant, the transformation of the local lift force l_j^n from $O_{NA^{(L)},j}$ to $O_{A^{(L)}}$ is computed by the following transformation matrix

$$\mathbf{T}_{A^{(L)}NA^{(L)},j} = \begin{bmatrix} 1 & 0 & 0 \\ 0 & \cos\Gamma_j & -\sin\Gamma_j \\ 0 & \sin\Gamma_j & \cos\Gamma_j \end{bmatrix} \tag{10}$$

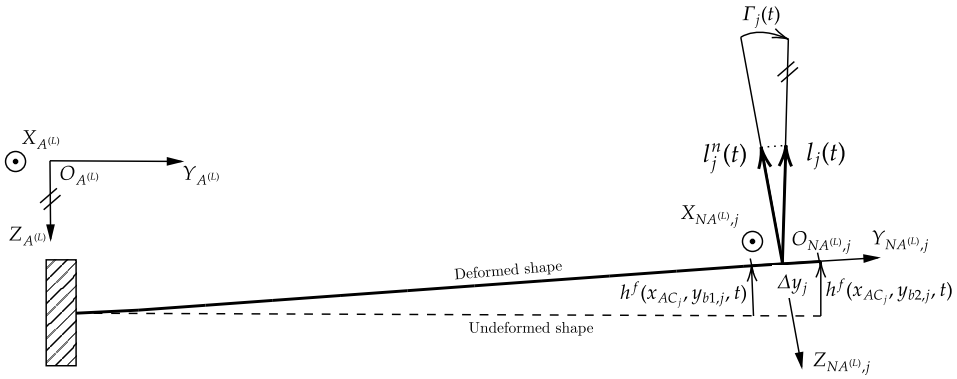

Figure 6: Right half span wing modeled as a cantilevered beam representing the deformation dihedral angle Γ_j between the LARF $O_{A^{(L)}}$ and and a LNARF $O_{NA^{(L)},j}$ corresponding to the jth strip.

5 RESULTS

The two TU-Flex (Section 2) configurations with FW and VFW set will be the reference aircrafts for the presented results. In the following, the considered formulations, detailed so far, will be compared in terms of stability analysis (root loci with increasing airspeed) and dynamic behaviour in time simulations.

5.1 Stability Analyses

The root loci of the TU-Flex aircraft model with FW and VFW set for the QLAM and ULAM has been computed. The chosen range of velocities is 18 m/s to 50 m/s, representing the TU-Flex flight envelope velocities described in [13]. In Fig. 7 and 8, the root loci varying the

velocity from 18 m/s to 50 m/s at the cruise flight altitude (100 m) of the TU-Flex with FW set using the QLAM and the ULAM is depicted respectively. The poles have been identified, following (in the case of the structural modes) the mode labels shown in Tab. 1. For the QLAM and ULAM, the velocity increase causes the migration of the poles of the structural modes towards the left-hand side of the pole map, influencing less the H1TI-W1ABI mode which remains at the same position for the velocity range. This migration is greater for the QLAM. The rigid body modes (Pure Roll, Short Period, Dutch Roll, Phugoid and Spiral) migrate the same magnitude varying the velocity for the QLAM and ULAM. Increasing the velocity, the Spiral mode and Pure Roll (PR) move towards the left-hand side of the pole map, becoming more stable. The Dutch Roll (DR) mode and Short Period (SP) mode increase their damped frequency while the one of Phugoid mode decreases.

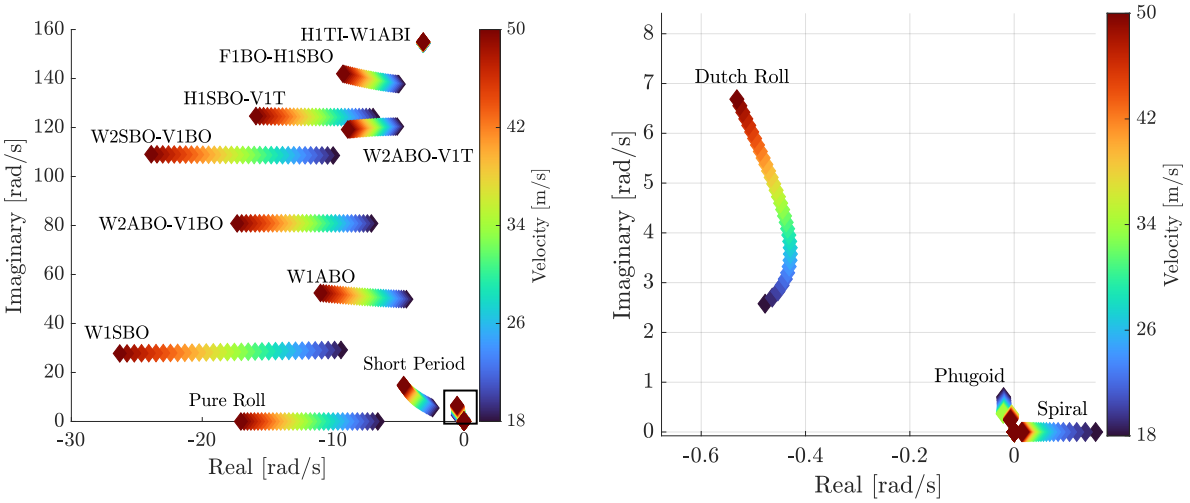

Figure 7: Full root loci varying the velocity from 18 m/s to 50 m/s at the cruise flight altitude of the TU-Flex with FW set using QLAM (left) and a zoomed-in view near the origin (right).

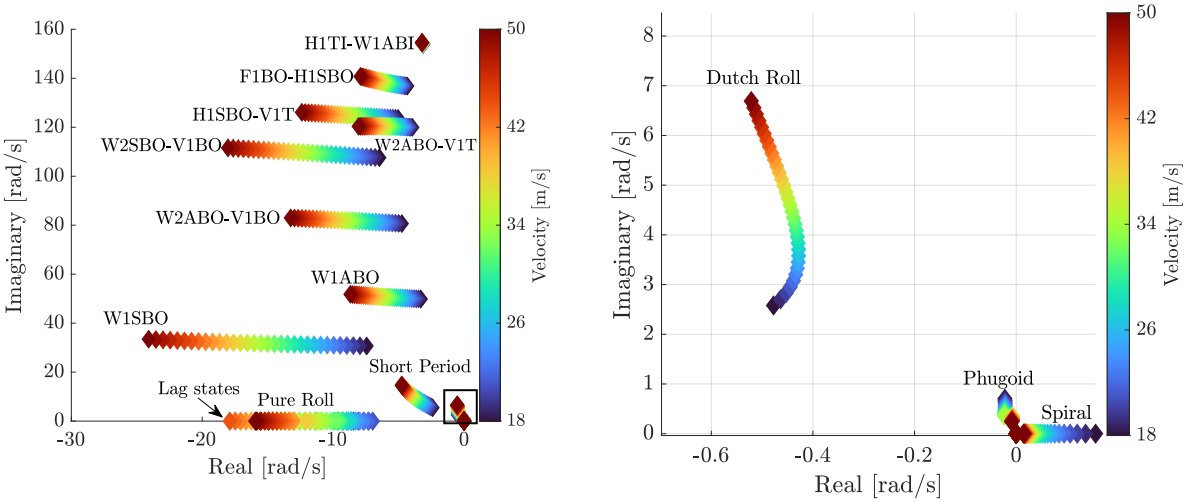

Figure 8: Full root loci varying the velocity from 18 m/s to 50 m/s at the cruise flight altitude of the TU-Flex with FW set using ULAM (left) and a zoomed-in view near the origin (right).

In Fig. 9 and 10, the root loci varying the velocity from 18 m/s to 50 m/s at the cruise flight altitude (100 m) of the TU-Flex with VFW set using the QLAM and the ULAM is depicted respectively. The poles have been identified, following (in the case of the structural modes) the mode labels shown in Tab. 2. For the QLAM and the ULAM, increasing the velocity, the

poles of the structural modes move towards the left-hand side of the pole map, less the W1SBI-W2SBO mode which remains at the same position for the velocity range. As for the TU-Flex with FW set, this migration is more pronounced for the QLAM. For both formulations (QLAM and ULAM), the airspeed increase yields a migration of the modes Spiral, DR and PR towards the left-hand side of the pole map. The PR mode for the ULAM has an oscillatory behaviousr. The Phugoid mode damped frequency decreases while the one from the SP mode increases. This higher damped frequency of the SP mode increases the coupling with the W1SBO structural mode, in particular for the velocity range from 26 m/s to 34 m/s. Furthermore, the W2ABO mode and SP mode get closer while increasing the velocity. These coupling mechanisms between SP rigid body mode and the W1SBO and W2ABO structural modes were not found in Fig. 7 and 8 for the TU-Flex with FW set.

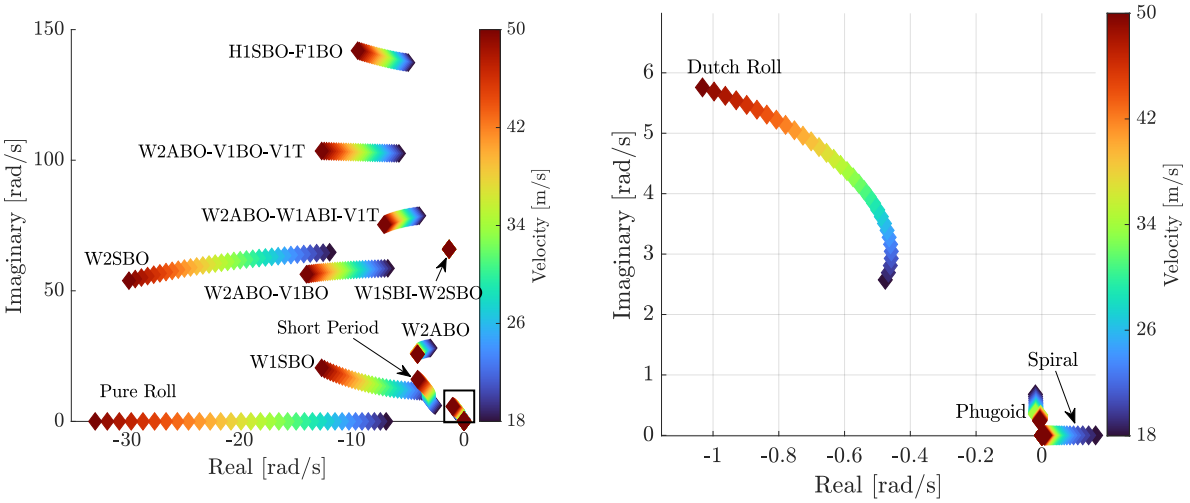

Figure 9: Full root loci varying the velocity from 18 m/s to 50 m/s at the cruise flight altitude of the TU-Flex with VFW set using QLAM (left) and a zoomed-in view near the origin (right).

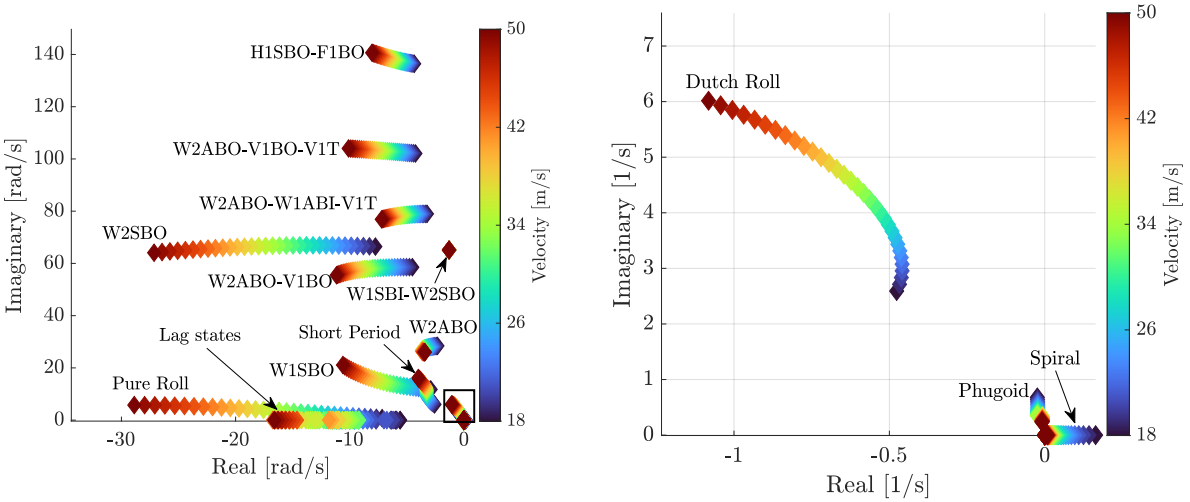

Figure 10: Full root loci varying the velocity from 18 m/s to 50 m/s at the cruise flight altitude of the TU-Flex with VFW set using ULAM (left) and a zoomed-in view near the origin (right).

In Fig. 11 and 12 the Modal Assurance Criterion (MAC) map of the TU-Flex with FW and VFW set is depicted respectively. The MAC map represents the degree of consistency between a normalized mode and a system state. A MAC value close to 1 indicates that the normalized mode is high correlated with a certain system state, whereas a value close to 0 indicates low

correlation. The MAC map has been computed for 22 and 30 m/s at the cruise flight altitude (100 m) using the ULAM. For Fig. 11 and 12 the represented system states (y-axis) are the first eighth modes shapes η and its derivatives $\dot{\eta}$, and the rigid body states: velocity V; pitch angle Θ; angle of attack α; pitch rate q; slide slip angle β; yaw rate r; roll angle Φ; and roll rate p. Regarding the x-axis, in Fig. 11 the structural modes of the Tab. 1 and the rigid body modes (SP, PR, Phugoid, DR and Spiral) are represented.

The correlation value MAC of the rigid body modes (SP, PR, Phugoid, DR and Spiral) with the modes shapes η and its derivatives $\dot{\eta}$ shows the coupling between the rigid body modes and the structural modes. For the TU-Flex with FW set in Fig. 11, the Spiral mode is only influenced by the lateral-directional rigid body states r, Φ and β. The DR mode has influence of the lateral-directional rigid body states r, p and β, and it is highly correlated with the modal shape η_8, obtaining a MAC equals 0.62. This η_8 corresponds to the eighth mode V1T-W1ABI, being V1T mode contribution which causes this coupling. The Phugoid mode is influenced by the longitudinal rigid body states V, Θ and q, and the first modal shape η_1 which corresponds to the W1SBO mode. The PR mode is correlated by the lateral rigid body state p, and the modal shapes η_2 and η_6. The W1ABO mode (η_2) and the mode contribution V1T from η_6 influence on the roll aircraft motion. The SP mode is correlated with the longitudinal rigid body states V, Θ and q, and the modal shapes η_1 and η_7 and the modal shape derivative $\dot{\eta}_1$. The coupling consists of the rigid body SP mode with the structural modes W1SBO (η_1 and $\dot{\eta}_1$) and H1SBO contribution from η_7. The MAC value of the SP mode with $\dot{\eta}_1$ is 0.65. Regarding the correlation of the modes shapes and its derivatives with themselves, remark the coupling of the fifth structural mode W2ABO-V1T with the sixth structural mode H1SBO-V1T through their corresponding modes shape derivatives $\dot{\eta}_5$ and $\dot{\eta}_6$ respectively. Part of their modal shape consists of the V1T mode, and they have similar natural frequency values (Tab. 1). Increasing the velocity from 22 m/s to 30 m/s, no significant changes are obtained. The MAC of the DR mode with η_8 decreases to 0.52.

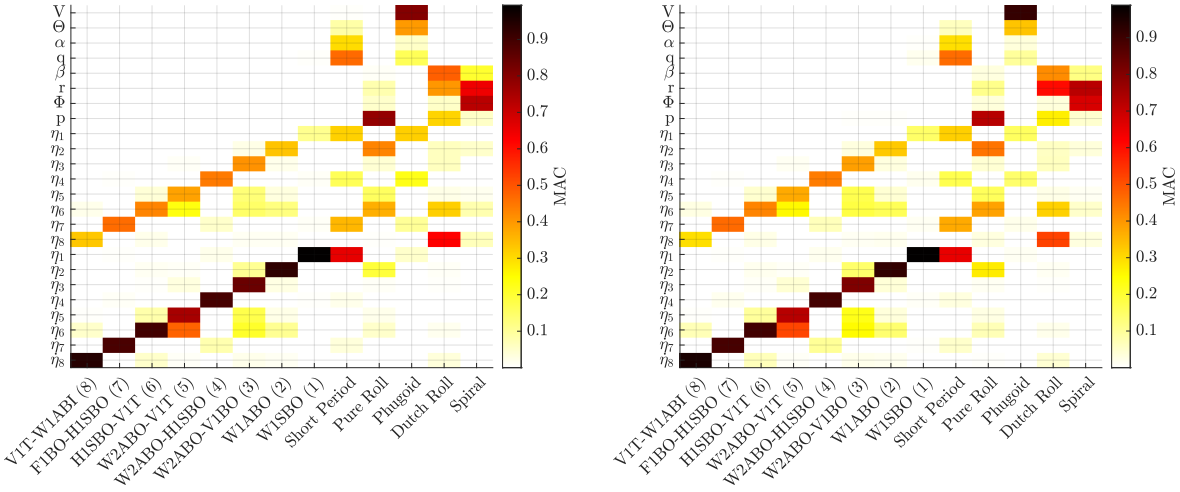

Figure 11: MAC map of the TU-Flex with FW set at 22 m/s (left) and 30 m/s (right), at the cruise flight altitude (100 m).

In Fig. 12, for the TU-Flex with VFW set, the influence of the rigid body states on the rigid body modes follow the same correlation as for the TU-Flex with FW set (Fig. 11). Focusing on the coupling of the rigid body modes with the structural modes, the DR mode is influenced by the modal shape η_6 due the contribution of the V1T of the sixth structural mode (H1SBO-V1T). The

MAC value is 0.65. The Phugoid mode is structurally influenced by the modal shapes η_1, η_4 and η_5, corresponding to the structural modes W1SBO, W1SBI-W2SBO and W2SBO respectively. The PR mode is correlated with η_3, η_6 and η_7, corresponding to the structural modes W2ABO-V1BO, W2ABO-W1ABI-V1T and W2ABO-V1BO-V1T respectively. The highest correlations belong to W2ABO-W1ABI-V1T and W2ABO-V1BO-V1T modes with a MAC value at 22 m/s equals 0.57 and 0.47 respectively. The SP mode is mainly correlated with the first modal shape η_1 and its derivative $\dot{\eta}_1$ which corresponds to the W1SBO mode. The MAC value for the correlation with $\dot{\eta}_1$ at 22 m/s is 0.73. Regarding the coupling between structural modes, it exists an influence of the derivative of the fifth modal shape $\dot{\eta}_5$ on the derivative of the fourth modal shape $\dot{\eta}_4$ and vice versa. They are modes that share the W2SBO mode contribution, with similar natural frequency values (Tab. 2). Increasing the velocity from 22 m/s to 30 m/s, the correlation of the SP mode with the first modal shape derivative $\dot{\eta}_1$ increases a 12%. In the case of the Phugoid mode, the correlation with the modal shapes η_4 and η_5 decreases a 50%.

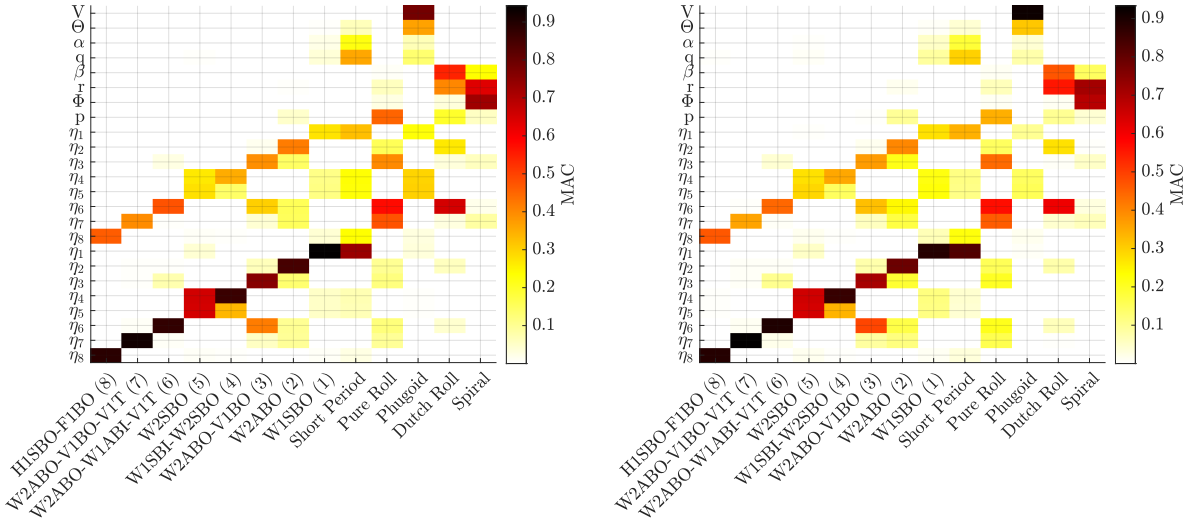

Figure 12: MAC map of the TU-Flex with VFW set at 22 m/s (left) and 30 m/s (right), at the cruise flight altitude (100 m).

In summary, increasing the flexibility level of TU-Flex (from FW to VFW configuration) increases more importantly the coupling of SP mode and the W1SBO mode. The increase on velocity for the TU-Flex VFW emphasize this coupling mechanism.

5.2 Simulation study cases

The time response simulations for several load cases within the TU-Flex flight envelope [13] will be presented in this section. The results using the five aerodynamic models described in Section 4.2 will be compared, considering the TU-Flex with FW and VFW set. Longitudinal manoeuvres will be considered, reaching certain load factor through elevator deflection δ_e. In Fig. 13 the TU-Flex flight envelope with the simulated study cases for this paper is depicted. Comparing with the flight envelope shown in [13], the maximum and minimum load factor has been reduced to 2.5g and -1g. Furthermore, from the cruise velocity V_C equals 30 m/s to the diving velocity V_D equals to 50 m/s a line has been drawn, limiting the negative load factor for that range of velocities. These modifications have been carried out according to the load factors planned to be reached during flight tests.

The manoeuvres correspond to an elevator input following the concept of 3211 input. This

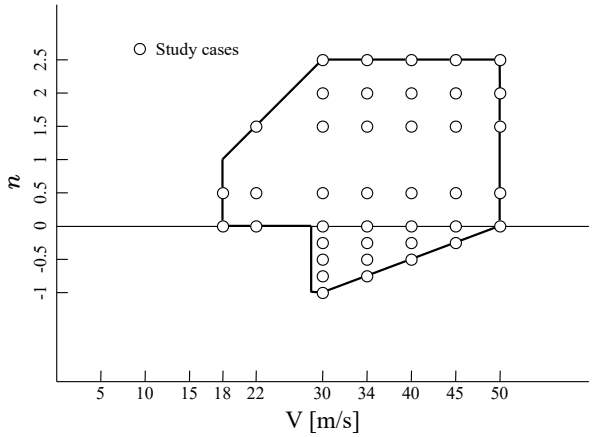

Figure 13: TU-Flex flight envelope with the simulated study cases for this paper.

type of input consists of 2 consecutive doublets, implementing four steps (composing the two doublets) of duration 3 sec, 2 sec, 1 sec and 1 sec respectively. These steps have the same amplitude. This type of input has been chosen due to the possibility of simulating for the same manoeuvre a content of variable frequency. In Fig 14 an elevator input example of the manoeuvres implemented for the study cases of Fig. 13 is represented. For the present study the duration of each step has been modified from the typical 3221 manoeuvre to 1.5 sec, 1 sec, 0.5 sec and 0.5 sec with the purpose of simulating higher frequencies inputs closer to the SP mode and W1SBO mode of the TU-Flex with VFW set (Tab. 2). Besides the amplitude of those steps has been modified, using the first step deflection $\Delta\delta_e/3$ to gain energy and being able to reach the corresponding load factor with the second step $\Delta\delta_e$ with less magnitude of deflection. Then, the last two steps $\Delta\delta_e/2$ and $\Delta\delta_e/6$ decrease their amplitudes, reaching the initial amplitude deflection progressively and not increasing loads and remaining within the flight envelope. The manoeuvre design has been carried out tuning the increment elevator deflection $\Delta\delta_e$ which reaches the corresponding load factor of the study case at a certain velocity.

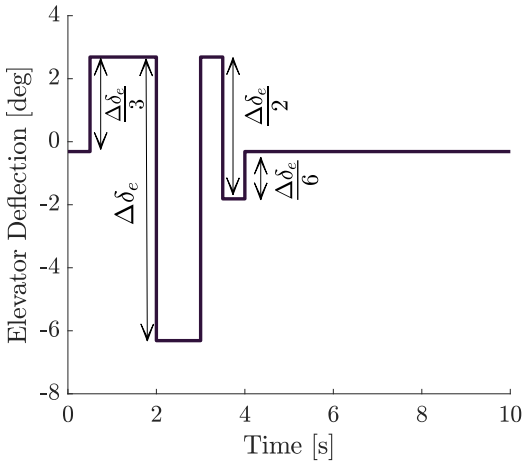

Figure 14: Elevator input manoeuvre for the study cases of the present paper.

From all the simulated study cases (Fig. 13), this paper will focus on the results obtained for the load cases 0g at 22 m/s and 1.5g at 30 m/s starting from 1g trimming condition. These study cases have been chosen with the requirement of representing an overview of what occur for the other study cases. Same flight envelope points will be discussed for the TU-Flex with FW and VFW set, using the five aerodynamics models described in Section 4.2.

5.2.1 Load case 1.5g at 30 m/s

The results of the load case 1.5g at cruise velocity 30 m/s and 100 meters altitude for the TU-Flex with FW and VFW using the five aerodynamic models described in Section 4.2 are represented in this section. In Fig. 15 the nonlinear response and elevator deflection for the TU-Flex with FW set using the QLAM, ULAM, UQNAM, USAM and USFAM is depicted. The longitudinal rigid body states V (velocity), H (altitude), α (AoA), q (pitch rate), Θ (pitch angle), elevator deflection (δ_e), and the wingtip vertical displacement and tip twist angle are represented. From a trimming condition at 30 m/s and 0.86^o of AoA, a first increment of elevator deflection $\Delta\delta_e/3$ (referring to the magnitude represented in Fig. 14) equals 3^o (maximum deflection of 2.7^o) is implemented at the time instant 0.5 sec. This first step allows to start the 1.5g manoeuvre at the time instant 2 sec with -0.42^o of AoA and a velocity of 30.6 m/s, performing a $\Delta\delta_e$ equals -9^o. The increment of AoA due the negative elevator deflection at 2 sec yields an increase of aerodynamic loads. A raise on the wingtip vertical displacement is produced, obtaining a maximum displacement of 11.4% for the QLAM and ULAM. For the UQNAM, USAM and USFAM the maximum wingtip vertical displacement is 10.9%. Overall, for this low level of flexibility, all formulations lead to similar results, and not considering aerodynamic nonlinearities overestimates deformations, as the comparison of peaks in wingtip vertical displacements reveals.

In Fig. 16 the nonlinear response and elevator deflection for the TU-Flex with VFW set using the QLAM, ULAM, UQNAM, USAM and USFAM is depicted. The longitudinal rigid body states V, H, α, q, Θ, elevator deflection, and the wingtip vertical displacement and wingtip twist angle are represented. From a trimming condition at 30 m/s and 1.34^o of AoA, a first increment of elevator deflection $\Delta\delta_e/3$ equals 3^o (maximum deflection of 0.33^o) is implemented at 0.5 sec. Thus the 1.5g manoeuvre starts at 2 sec with 0^o of AoA and a velocity of 30.6 m/s, performing a $\Delta\delta_e$ equals -10^o (total δ_e equals -9.66^o). The behaviour of the represented variables is the same as for the Fig. 15. The UQNAM and USAM obtain a maximum wingtip vertical displacement of 26.6% whereas the QLAM, ULAM and USFAM reach a maximum of 25%. At low AoA there is an underestimation of the local cl_α for the linear aerodynamics models (Fig. 5), reaching lower local lift force and vertical displacement. For the USFAM the applied lift force does not consider the axial contribution due to the bending out-of-plane, obtaining lower deformations. The wingtip twist angle decreases to -5.1^o for the UQNAM, USAM and USFAM whereas the QLAM and ULAM obtain -4.7^o.

The represented variables for the TU-Flex with FW set and with the VFW set follow the same tendency to the same load case with equal elevator input. The variables time responses of the VFW reach higher amplitudes, in particular for the structure parameters. The maximum vertical displacement of the TU-Flex VFW configuration is 58% higher than for the FW configuration. The minimum twist angle for the VFW configuration is 54% smaller. The five aerodynamic models compute the values of the longitudinal rigid body states nonlinear time responses with less than 1% of difference between formulations for the FW and VFW configuration. Regarding the structure parameters (vertical displacement and twist angle) for the FW configuration, the linear aerodynamic models (QLAM and ULAM) compute a maximum vertical displacement 5% greater than for the UQNAM, USAM and USFAM. For the VFW configuration, the tendencies between models are the same obtaining differences in maximum wingtip vertical displacement and twist angle up to 5%.

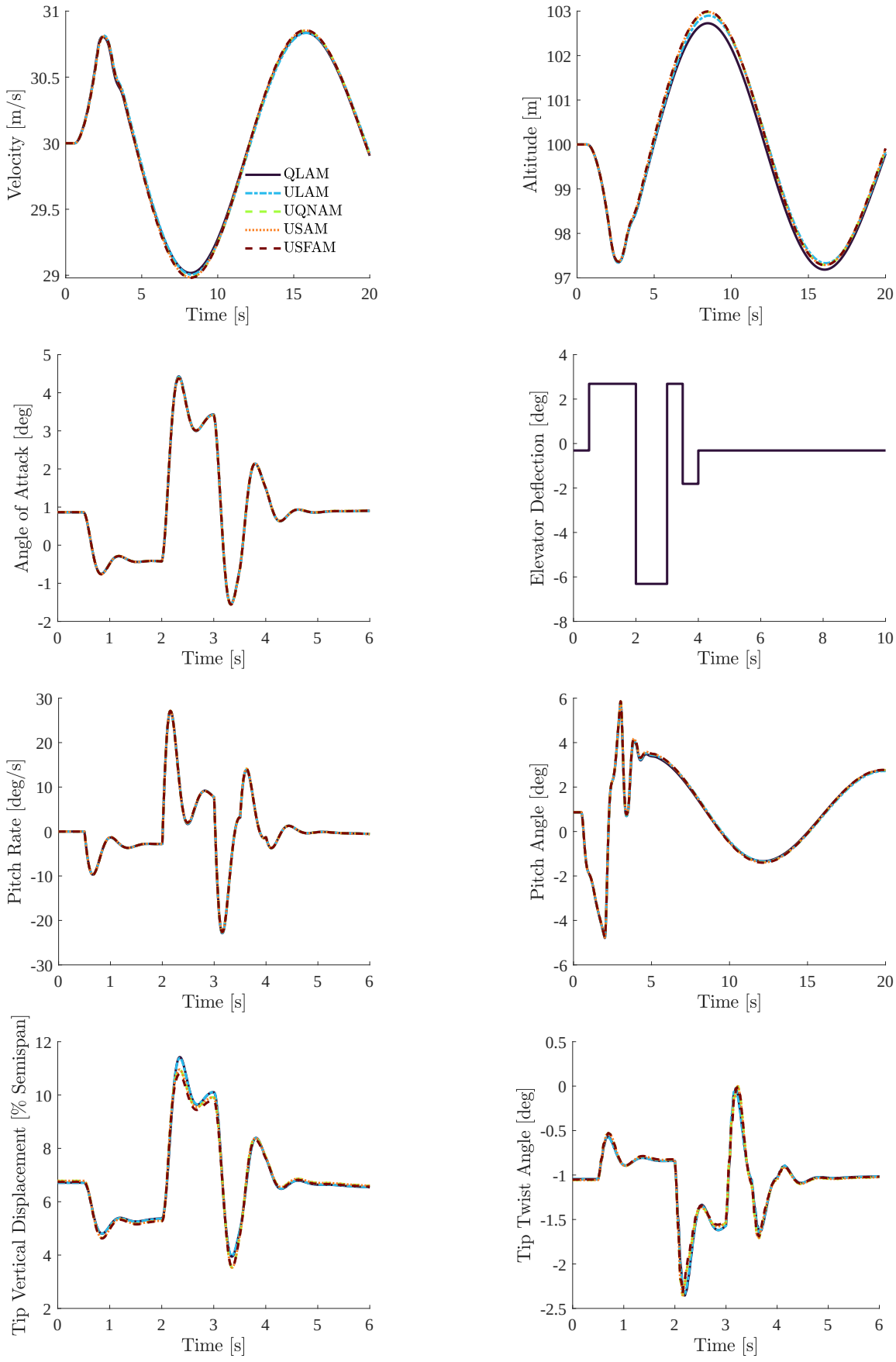

Figure 15: TU-Flex with FW set nonlinear response and elevator deflection for a load case of 1.5g at 30 m/s using the QLAM, ULAM, UQNAM, USAM and USFAM.

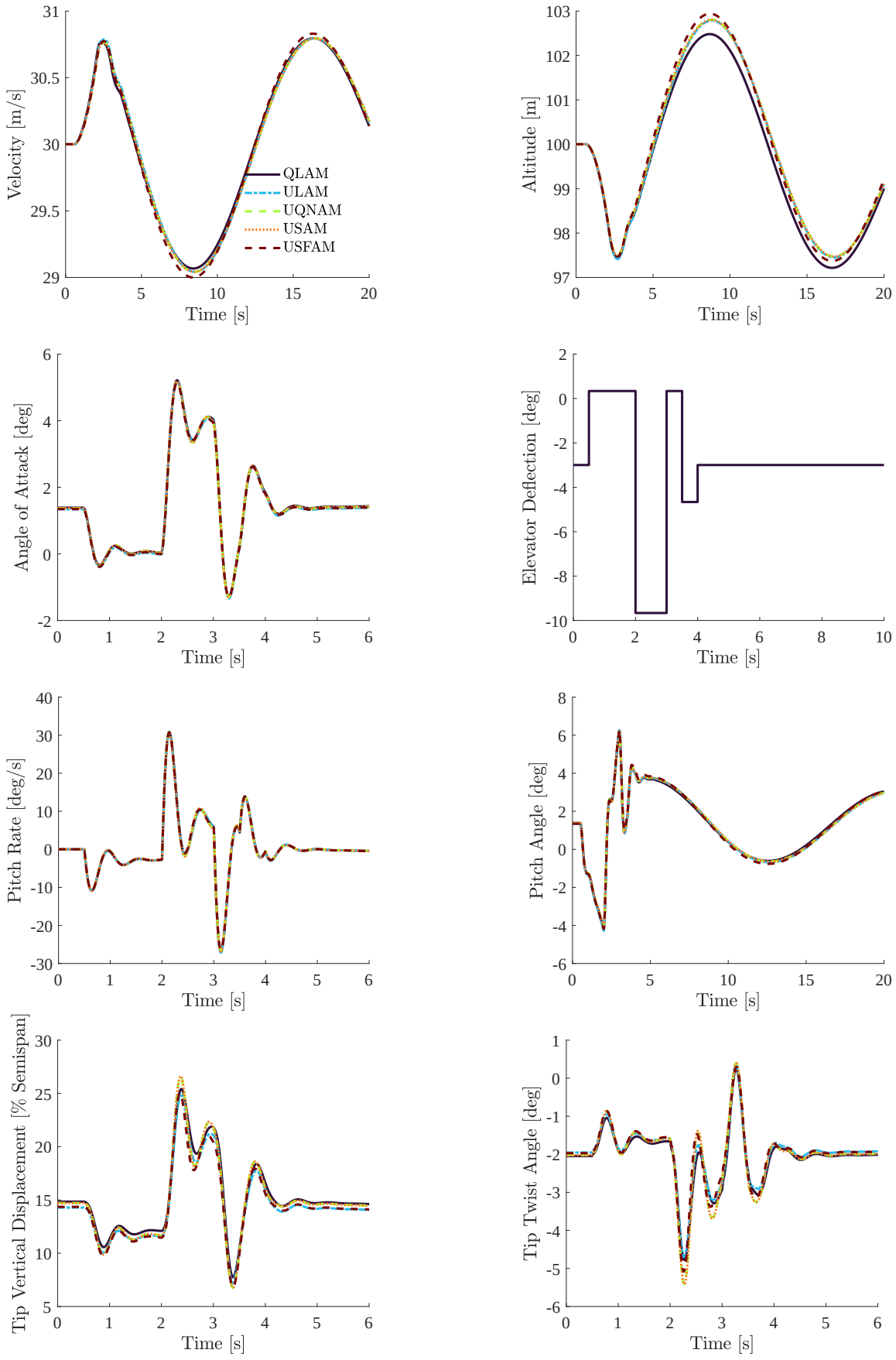

Figure 16: TU-Flex with VFW set nonlinear response and elevator deflection for a load case of 1.5g at 30 m/s using the QLAM, ULAM, UQNAM, USAM and USFAM.

5.2.2 Load case 0g at 22 m/s

The results of the load case 0g at low velocity 22 m/s and 100 meters altitude for the TU-Flex with FW and VFW using the five aerodynamic models described in Section 4.2 are represented in this section. In Fig. 15 the nonlinear response and elevator deflection for the TU-Flex with FW set using the QLAM, ULAM, UQNAM, USAM and USFAM is depicted. The same previous load case variables are represented. From a trimming condition at low velocity 22 m/s, AoA 6.4^o and elevator deflection -12^o, an increment elevator deflection step $\Delta\delta_e/3$ of -9^o at 0.5 sec is implemented. This deflection yields an increase of AoA to 11.2^o for the QLAM and ULAM, 10.9^o using the UQLAM and 10.8^o for the USAM and USFAM. At this level of AoA the linear aerodynamic models (QLAM and ULAM) differ significantly with UQNAM, USAM and USFAM (Fig. 5). Besides the USFAM and USAM start taking different values of cl_α comparing with UQNAM. Thus an overestimation of the aerodynamic forces is yielded by the QLAM, ULAM and UQNAM compared with the USAM and USFAM.

This overestimation of cl_α is also observed on the wingtip vertical displacement at the trimming point. The linear aerodynamic models (QLAM and ULAM) start the simulation at 7.7$\%$ of vertical displacement whereas the UQNAM, USAM and USFAM reach 6.7$\%$. The trimming wingtip twist angle for all the models is -2.4^o. The increment of AoA due the elevator deflection at 0.5 sec increases the wingtip vertical displacement for the linear aerodynamics models (QLAM and ULAM) to 10.7^o. Nevertheless, the UQNAM starting with cl_α equals 5.5 (rad)$^{-1}$ for 4^o AoA at the tip (sum between the twist angle due deformation and the rigid body AoA), the increment in AoA to 10.8^o decreases cl_α at the tip to 2.9 (rad)$^{-1}$. Therefore the lift force and wingtip vertical displacement reduces. This reduction in wingtip vertical displacement is also obtained for the USAM and USFAM, reaching a cl_α at the tip equals 1 (rad)$^{-1}$ at 10.8^o in AoA. Thus, this reduction in cl_α decreases the lift force for the UQNAM, USAM and USFAM reducing the wingtip vertical displacement.

The rigid body AoA reaches a maximum and start decreasing, reducing the local tip AoA and thus raising again the cl_α at the tip. The lift force is then changing its value, producing weakly damped oscillations on the wingtip vertical displacement, wingtip twist angle, pitch rate and rigid body AoA for the USAM and USFAM, and not captured by the other formulations. Using the oscillation period, a frequency oscillation equals 4.7 Hz is obtained from the wingtip vertical displacement subfigure. From Fig. 8 the W1SBO damped frequency oscillation at 22 m/s equals 4.9 Hz is observed. In the beginning, the oscillation amplitudes of the wingtip vertical displacement are 3$\%$ greater for the USAM. Nevertheless, the maximum value of wingtip vertical displacement during the oscillations is 11.3$\%$ for USFAM and 10.4$\%$ for USAM. These oscillations are not obtained for the linear aerodynamic models (QLAM and ULAM) neither UQNAM. Analyzing the pitch rate after the first positive increment due to the negative step deflection on the elevator, oscillations from 1 sec to 2 sec for the USAM and USFAM are observed.

In Fig. 18, a zoomed-in view of the pitch rate for that time range 1 sec to 2.5 sec is shown. The pitch rate time response for the USAM and USFAM is oscillating at frequency 5.18 Hz. The maximum pitch rate during oscillation for the USAM and USFAM is 8.49 deg/s whereas the maximum at 1.6 sec for the linear aerodynamic models (QLAM and ULAM) and UQNAM is 7 deg/s.

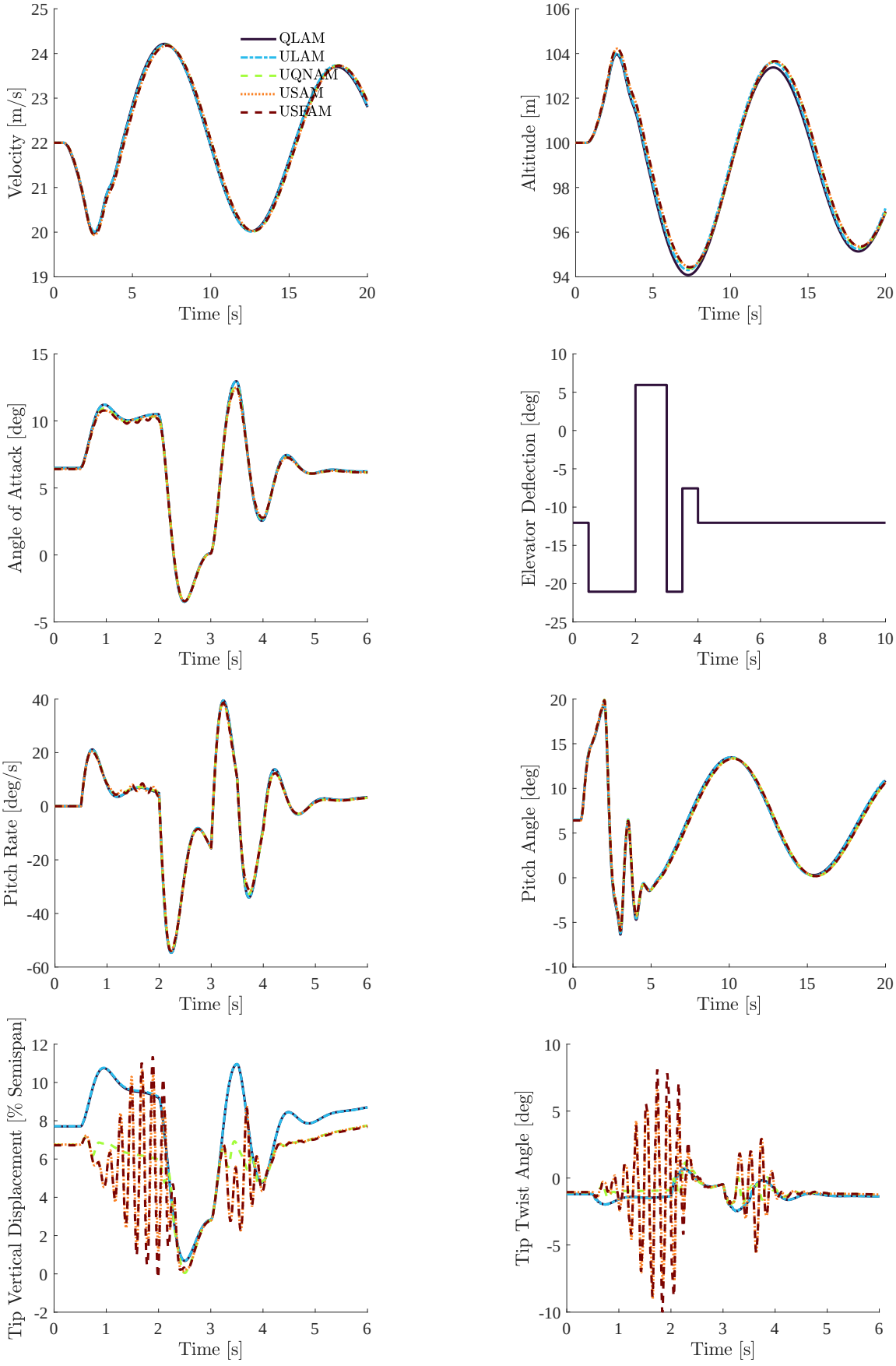

Figure 17: TU-Flex with FW set nonlinear response and elevator deflection for a load case of 0g at 22 m/s using the QLAM, ULAM, UQNAM, USAM and USFAM.

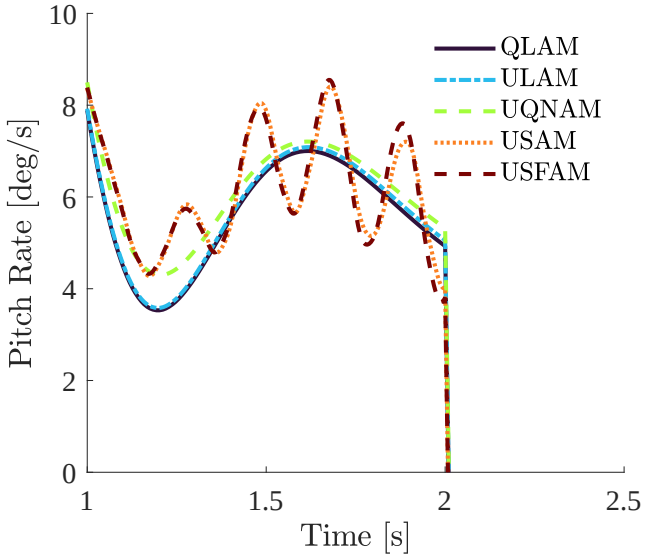

Figure 18: Zoomed-in view of the pitch rate from Fig. 17 for the time range 1 sec to 2.5 sec.

In Fig. 19 the nonlinear response and elevator deflection for the TU-Flex with VFW set using the QLAM, ULAM, UQNAM, USAM and USFAM is depicted. Similarly to the FW configuration, weakly damped oscillations due to stall effects appear, which could be captured only by the formulations with aerodynamic nonlinearity. In Fig. 20 the zoomed-in view of the angle of attack for the time range from 0.5 sec and 2.5 sec is depicted. Two frequency oscillations can be observed. Taking two oscillation peaks, there is a high frequency oscillation of approximated 12 Hz, and a low frequency oscillation of approximated 1.6 Hz. For this VFW configuration of the TU-Flex, at 22 m/s the damped frequency of the SP mode is 1.19 Hz, the W1SBO 1.94 Hz and the W2ABO-W1ABI-V1T 12.55 Hz. This interaction structure and rigid body also affects the pitch angle, velocity and altitude. The maximum value is 22.3^o for the UQNAM, USAM and USFAM, and 20.4^o for the QLAM aand ULAM. The velocity reaches a minimum value of 20 m/s for the QLAM and ULAM whereas for the UQNAM, USAM and USFAM the value is 19.6 m/s. The altitude maximum value is 104 meters for the QLAM and ULAM whereas for the UQNAM, USAM and USFAM is 104.7 meters.

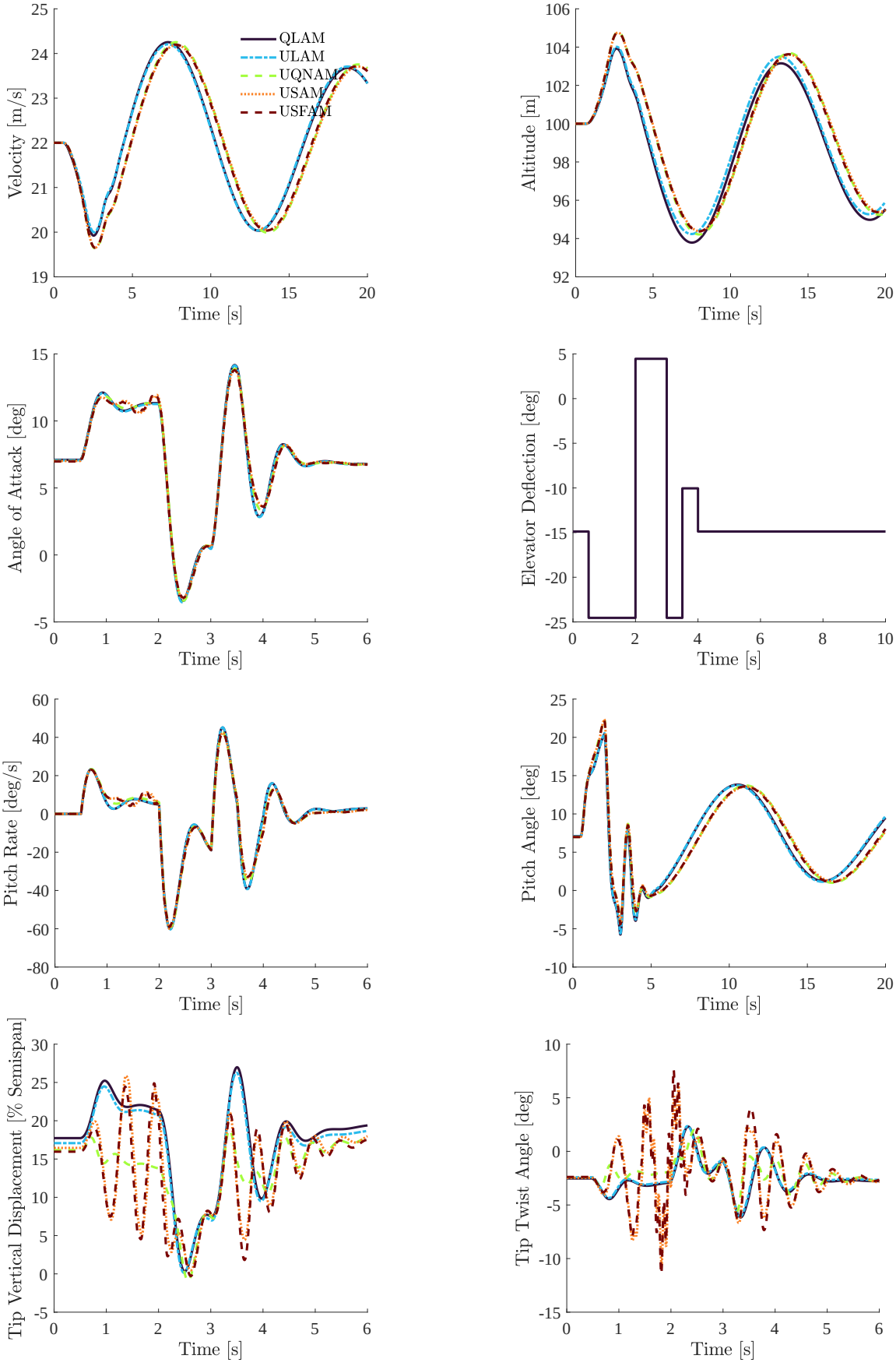

Figure 19: TU-Flex with VFW set nonlinear response and elevator deflection for a load case of 0g at 22 m/s using the QLAM, ULAM, UQNAM, USAM and USFAM.

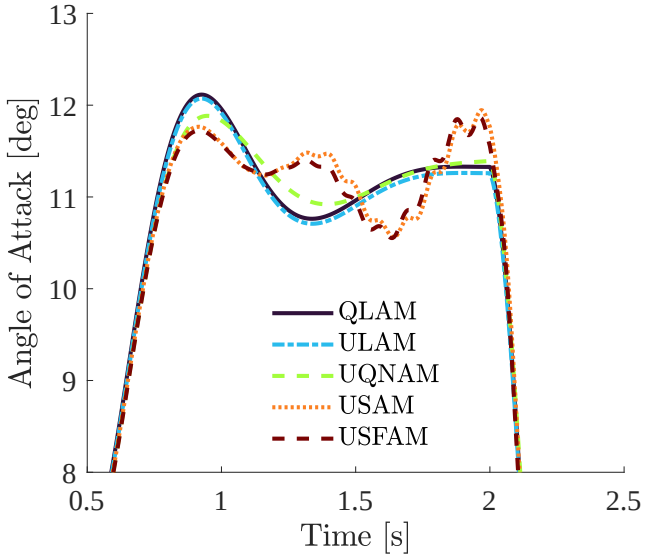

Figure 20: Zoomed-in view of the angle of attack from Fig. 19.

5.2.3 Summary

The relevant differences obtained by these studies are focused on the consideration of stall effects. Oscillations on the lift force due to changes on the local cl_α yield low damped vibrations on the vertical displacement. This vertical displacement oscillations interact with the rigid body producing changes on the AoA and pitch rate. This impact of stall effects on the dynamic behaviour (captured by USFAM and USAM) affected the orange points from the considered points in TU-Flex flight envelope, for both configurations, depicted in Fig. 21, i.e. in a vast part of the flight envelope there is an important stability problem that may be hidden by applying linear aerodynamic formulations. This conclusion is emphasised by the increase in flexibility.

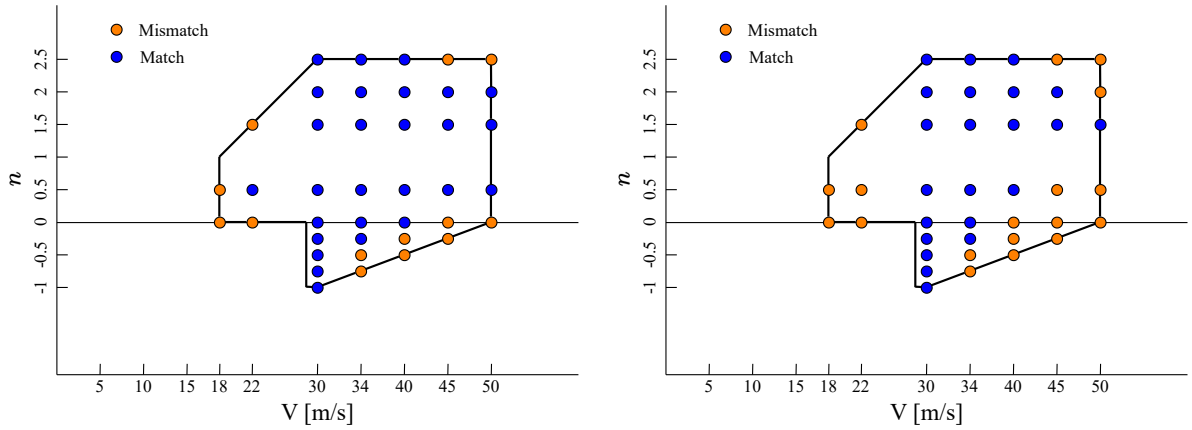

Figure 21: TU-Flex flight envelope representing the mismatch due to considering stall with the FW set (left) and VFW set (right).

6 CONCLUDING REMARKS

This paper has studied the influence of local nonlinear aerodynamics on the TU-Flex aircraft model for its two flexibility levels. Analyzing the dynamic behaviour of these two configurations, the follower forces effect does not have a significant impact while considering geometrically linear structure (not capturing structure shortening and curvature effects). Nevertheless, stall effects influence the TU-Flex (flexible and very flexible configuration) dynamic behaviour

by the coupling rigid body and structure, not captured by the linear aerodynamic models. Thus, in a vast part of the flight envelope there is an important stability problem that may be hidden by applying linear aerodynamic formulations. This stability problem is emphasised by the increase in flexibility due to larger deformations and stronger coupling. In the stability analysis, it was concluded that the coupling of short period and wing first bending mode is 20% greater for the TU-Flex very flexible configuration.

7 ACKNOWLEDGEMENTS

This study was financed in part by the German Federal Ministry for Economic Affairs and Climate Action (BMWK) due to a resolution of the German Federal Parliament within the scope of the LuFo VI-2 project FlexFuture (Grant number 20E2120A).

8 REFERENCES

[1] Afonso, F., Vale, J., der Oliveira, et al. (2017). A review on non-linear aeroelasticity of high aspect-ratio wings. *Progress in Aerospace Sciences*, 89, 40–57. ISSN 0376-0421. doi:https://doi.org/10.1016/j.paerosci.2016.12.004.

[2] Waszak, M. R. and Schmidt, D. K. (1988). Flight dynamics of aeroelastic vehicles. *Journal of Aircraft*, 25(6), 563–571. doi:10.2514/3.45623.

[3] Silvestre, F. and Paglione, P. (2008). *Dynamics and Control of a Flexible Aircraft*. AIAA Atmospheric Flight Mechanics Conference and Exhibit. doi:10.2514/6.2008-6876.

[4] Van Schoor, M. C. and von Flotow, A. H. (1990). Aeroelastic characteristics of a highly flexible aircraft. *Journal of Aircraft*, 27(10), 901–908.

[5] Patil, M. J. and Hodges, D. H. (2006). Flight dynamics of highly flexible flying wings. *Journal of Aircraft*, 43(6), 1790–1799. doi:10.2514/1.17640.

[6] Noll, T. E., Brown, J. M., Perez-Davis, M. E., et al. (2004). Investigation of the helios prototype aircraft mishap volume i mishap report. *Downloaded on*, 9, 2004.

[7] Hodges, D. H. (1990). A mixed variational formulation based on exact intrinsic equations for dynamics of moving beams. *International journal of solids and structures*, 26(11), 1253–1273.

[8] Hodges, D. H. (2003). Geometrically exact, intrinsic theory for dynamics of curved and twisted anisotropic beams. *AIAA journal*, 41(6), 1131–1137.

[9] Peters, D. A. and Johnson, M. J. (1994). Finite-state airloads for deformable airfoils on fixed and rotating wings. *Asme-Publications-AD*, 44, 1–1.

[10] Patil, M. J., Hodges, D. H., and Cesnik, C. E. S. (2000). Nonlinear aeroelastic analysis of complete aircraft in subsonic flow. *Journal of Aircraft*, 37(5), 753–760. doi:10.2514/2.2685.

[11] Su, W. and Cesnik, C. E. S. (2011). Dynamic response of highly flexible flying wings. *AIAA Journal*, 49(2), 324–339. doi:10.2514/1.J050496.

[12] Riso, C. and Cesnik, C. E. (2023). *Investigation of Geometrically Nonlinear Effects in the Aeroelastic Behavior of a Very Flexible Wing*. doi:10.2514/6.2023-0759.

[13] González, P., Stavorinus, G., Silvestre, F. J., et al. (2023). *TU-Flex: A Very-Flexible Flying Demonstrator with a Generic Transport Aircraft Configuration*. AIAA SCITECH Forum. doi:10.2514/6.2023-1312.

[14] Gonzáles, P. J., Quesada, A. A. G., Barbosa, G. C., et al. (2024). Wind tunnel testing and modal validation of tu-flex's high aspect ratio wings. In *21th International Forum on Aeroelasticity and Structural Dynamics, IFASD 2024*.

[15] NASA. Openvsp. `https://openvsp.org/`. Retrieved on: 2024.

[16] Altair hypermesh. `https://altair.com/hypermesh`. Retrieved on: 2024.

[17] González, P. J., Stavorinus, G., Sahin, H., et al. (2022). A structural preliminary design of a flexible flying demonstrator. In *33rd Congress of the International Council of the Aeronautical Sciences, ICAS 2022*.

[18] Klimmek, T. (2009). Parameterization of topology and geometry for the multidisciplinary optimization of wing structures. In *CEAS 2009 - European Air and Space Conference*.

[19] Klimmek, T. (2014). Parametric set-up of a structural model for fermat configuration aeroelastic and loads analysis. *Journal of Aeroelasticity and Structural Dynamics*, 3(2). doi:10.3293/asdj.2014.27.

[20] González, P. J., Shahi, H., Meddaikar, M. Y., et al. (2022). Flexible-wing design process for tu-flex demonstrator. In *19th International Forum on Aeroelasticity and Structural Dynamics, IFASD 2022*.

[21] Barbosa, G. C., Quesada, A. A. G., Gonzáles, P. J., et al. (2024). Aeroservoelastic analysis and load alleviation control for very flexible aircraft: Tu-flex study. In *21th International Forum on Aeroelasticity and Structural Dynamics, IFASD 2024*.

[22] Silvestre, F. J. and Luckner, R. (2015). Experimental validation of a flight simulation model for slightly flexible aircraft. *AIAA Journal*, 53(12), 3620–3636. doi:10.2514/1.J054023.

[23] Schrder, B.-O., González, P. J., and Silvestre, F. J. (2022). A structural preliminary design of a flexible flying demonstrator. In *33rd Congress of the International Council of the Aeronautical Sciences, ICAS 2022*.

COPYRIGHT STATEMENT